REPORT

Structure of the 30S ribosomal decoding complex at ambient temperature

E. HAN DAO[1], FRÉDÉRIC POITEVIN[1,2], RAYMOND G. SIERRA[1,3], CORNELIUS GATI[2,4], YASHAS RAO[1,3], HALIL IBRAHIM CIFTCI[1], FULYA AKŞIT[1], ALEX MCGURK[3], TREVOR OBRINSKI[3], PAUL MGBAM[3], BRANDON HAYES[3], CASPER DE LICHTENBERG[5], FATIMA PARDO-AVILA[2], NICHOLAS CORSEPIUS[2], LINDSEY ZHANG[1], MATT SEABERG[3], MARK S. HUNTER[3], MENGLING LIANG[3], JASON E. KOGLIN[3], SOICHI WAKATSUKI[2,4] & HASAN DEMIRCI[1,2,4]

[1] Stanford PULSE Institute, SLAC National Laboratory, Menlo Park, California, USA
[2] Department of Structural Biology, Stanford University, Palo Alto, California, USA
[3] Linac Coherent Light Source, SLAC National Laboratory, Menlo Park, California, USA
[4] Biosciences Division, SLAC National Laboratory, Menlo Park, California, USA
[5] Institutionen för Kemi, Kemiskt Biologiskt Centrum, Umeå Universitet, Umeå, Sweden

ABSTRACT

The ribosome translates nucleotide sequences of messenger RNA to proteins through selection of cognate transfer RNA according to the genetic code. The decoding process of the ribosome has been extensively studied structurally at high resolution. Ribosome crystals are particularly sensitive to X-ray radiation, a difficulty that led to the development of data collection at cryogenic temperature, which is now the standard in macromolecular crystallography. Structural analysis of ribosomes using electron microscopy equally requires cryogenic cooling of the specimen. The advent of X-ray free electron lasers (XFELs) enabled to probe delicate crystals of ribosome complexes at ambient temperature, before they are destroyed by the fsec X-ray pulse. To explore the structural basis of ribosome decoding at near-physiological temperature, we determined the ambient-temperature X-ray crystal structure of the *Thermus thermophilus* 30S ribosomal subunit decoding complex to 3.45 Å resolution using data obtained at the Linac Coherent Light Source (LCLS). We found that the ambient-temperature structure was largely consistent with existing cryogenic-temperature crystal structures, with key residues of the decoding complex exhibiting similar conformations, including adenosine residues 1492 and 1493, which directly participate in decoding. However, small differences in our structure include an alternate conformation of cytosine 1397 near the mRNA channel and the A-site.

Keywords: Serial Femtosecond X-ray crystallography, ribosome, decoding, ambient temperature, antibiotics

Corresponding authors: hdemirci@stanford.edu and dao@stanford.edu

INTRODUCTION

The bacterial ribosome possesses universally conserved functional centers that are structurally dynamic and undergo local and large-scale conformational rearrangements during protein synthesis (Ogle et al. 2001; Petrov et al. 2011; Loveland et al. 2017). In particular, the small (30S) ribosomal subunit, which is responsible for decoding the messenger RNA sequence, undergoes rearrangement of the universally-conserved monitoring residues A1492 and A1493 in the decoding center, as well as a large-scale domain closure that involves movement of the body of the whole 30S subunit closer to helix 44 (Yoshizawa et al. 1999; Ogle et al. 2001; Demirci et al. 2013a). Although such conformational changes during translation have been identified, the current understanding of the structural dynamics of decoding still remains incomplete. (Ogle et al. 2003; Loveland et al. 2017).

X-ray crystallography performed at synchrotron light sources has revealed the structures of the ribosome complexes at high resolution (Ban et al. 2000; Schluenzen et al. 2000; Wimberly et al. 2000; Yusupov et al. 2001; Schuwirth et al. 2005; Korostelev et al. 2006; Selmer et al. 2006; Yusupova et al. 2006; Ben-Shem et al. 2011). A key aspect to this important achievement was the development of procedures to collect data at cryogenic temperature (Haas and Rossmann 1970; Evers et al. 1994), which enabled the acquisition of datasets from single crystals that contained sufficient high-resolution data to build high-resolution models (Warkentin et al. 2014). Electron microscopy performed at cryogenic temperature has added even more information about the ribosome during several steps of protein synthesis, at increasing resolution to an existing wealth of structural information spanning a large number of species and conformational states (Mitra et al. 2005; Fischer et al. 2015; Natchiar et al. 2017). Cooling ribosomal samples to cryogenic temperature mitigates the propagation of radiation damage by reducing the movement of radicals produced by irradiation with electrons or X-rays, lowering the thermal fluctuations and conformational distributions of side- and main-chain residues, and rigidifying the structure, partly through dehydration by adding hygroscopic cryo-protectants (Warkentin et al. 2014). Therefore, while it enables successful data collection, cryo-cooling can potentially mask important details about local and global conformational dynamics and allostery of the ribosome.

Nucleic acids generally are rather flexible and exhibit significant conformational fluctuations, enabling them to perform biological functions such as protein recognition, DNA replication, gene regulation and expression (Hagerman 1988; Hagerman 1990; Lebrun et al. 1997; Peters and Maher 2010; Tan and Chen 2011). Ribosomal RNA is no exception, and is of significant importance in our understanding of the functional relevance of nucleic acids (Noller 2013). Additionally, the structure and conformational

heterogeneity of RNA molecules are determined by the composition and physico-chemical state of its surrounding electrolytic medium (Anthony et al. 2012; Lipfert et al. 2014; Allred et al. 2017). Structural studies of ribosomes at temperatures closer to the physiological range could potentially reveal previously-obscured conformations and provide a means to evaluate their local dynamics and role in catalysis (Sierra et al. 2016).

In this work, we present an ambient-temperature structure of a 30S ribosomal decoding complex through a serial femtosecond X-ray crystallography (SFX) experiment. Using femtosecond-duration pulses, we obtain diffraction from microcrystals prior to the onset of radiation damage induced by the X-ray beam using an X-ray free-electron laser (XFEL). The microcrystals contained ribosomal subunits bound to a cognate mRNA-anticodon stem loop (ASL) complex and were introduced to the X-ray beam in a liquid suspension with an electrokinetic sample injector. We then compare our structure to analogous structures determined previously through synchrotron X-ray diffraction performed at cryogenic temperature, to identify the extent of differences between data collected at either temperature condition. Finally, we consider how ambient-temperature X-ray crystallography can further benefit the structural understanding of the ribosome complexes.

RESULTS AND DISCUSSION

SFX workflow for microcrystals of 30S ribosomal subunits

A brief overview of the experimental methods used for data collection follows, along with references to the pertinent subsections within the ***Materials & Methods***. Microcrystals of the 30S ribosomal subunit were soaked with 80 μM paromomycin, 200μM mRNA and 200 μM phenylalanine tRNA anticodon stem loop, ASL_{Phe} oligonucleotide, resulting in a slurry of 2 × 2 × 4 μm^3 size 30S decoding complex microcrystals (see ***Preparation and crystallization of 30S ribosomal subunits for SFX crystallography at an XFEL***). They were delivered to the X-ray beam at the Coherent X-ray Imaging (CXI) instrument (Liang et al. 2015) of the Linac Coherent Light Source (LCLS; Menlo Park, CA, USA) in a liquid suspension. Sample solution comprised of the unmodified mother liquor including 17% 2-methyl-2,4-pentanediol (MPD) and delivered via a concentric electrokinetic liquid injector (see ***coMESH construction*** and ***Operation of the coMESH***), as previously used for crystalline ribosome samples (Sierra et al. 2016) (Fig. 1A) (see ***Selecting a sister liquor for ribosome microcrystalline slurry*** and ***ribosome microcrystalline sample injection by using coMESH***). During a six-hour "protein crystal screening" beamtime, we collected a complete dataset extending to 3.45 Å-resolution (**Table 1**). A total of 1,731,280

109 detector frames were collected (corresponding to 240 minutes of net data collection time), of which
110 165,954 were identified as 'hits' and finally 19,374 diffraction patterns were successfully indexed and
111 merged into the final dataset. (see ***Data collection and analysis for SFX studies at LCLS*** and ***Ambient***
112 ***temperature 30S ribosomal subunit SFX structure refinement***).
113
114 **Decoding complex structure at ambient temperature**
115
116 In comparing the ambient-temperature structure with its equivalents at cryogenic temperature (PDB IDs:
117 1IBL and 4DR4) (Ogle et al. 2001; Demirci et al. 2013a), we found that the overall decoding crystal
118 structure was very similar to the cryogenic structures; however, we observed an alternate conformation of
119 mRNA channel residue C1397 (further discussed below). A least-squares alignment of all 17,056 16S
120 rRNA atoms in the 30S structures showed an overall RMSD of 0.45 and 0.62 Å between the new structure
121 and the cryogenic structures 4DR4 and 1IBL, respectively (Fig. 1B). The resulting electron density map
122 indicated good mRNA and ASL_{Phe} density quality in F_o-F_c difference electron density maps (Fig. 2A). The
123 crystal structure of the 30S decoding complex at ambient temperature adopted the canonical decoding
124 conformation, with the h44 residues A1492 and A1493 flipped out toward the minor groove of ASL and
125 mRNA pair, consistent with the cryogenic data (Fig. 2B). The minimal binding differences observed
126 between the cryogenic and ambient temperature 30S decoding complex structures (Figs. 1B, 2B-D)
127 suggest that ribosomal decoding complexes can be probed at cryogenic temperature and may still be
128 representative of what occurs at ambient temperature. However, we identified small differences within the
129 mRNA channel in the region between the S4-S5 protein interface and the 30S acceptor A-site.

130 **Structural perturbation in the mRNA channel**
131
132 In the structure presented here, the hydrogen bonding interactions of codon residues 1-3 of the hexauridine
133 in the mRNA-ASL complex were markedly similar to those observed in the cryogenic temperature crystal
134 structure, as shown by the clear positive difference density for each base pair in the omit F_o-F_c electron
135 density maps at 3.45 Å resolution (Fig. 3A-F). On the other hand, residues 4-6 of the hexa-uridine were
136 disordered and as a result not modeled in the cryogenic structure, while clear electron density was
137 observed in the ambient-temperature structure (Fig. 2A). Furthermore, the 16S rRNA residue C1397 was
138 captured in an alternate conformation, pointing away from the disordered hexauridine in the cryogenic
139 dataset and involved in a stabilizing interaction with the mRNA phosphate group of residue 4 in the
140 ambient-temperature structure (Fig. 4A-D).
141

The movement of the messenger RNA is controlled during the transition from pre- to post-translocation (Moazed and Noller 1989; Achenbach and Nierhaus 2015). The universally conserved bases C1397 and A1503 of the 16S rRNA head domain located on top of large secondary rRNA structures (Zhou et al. 2013; Achenbach and Nierhaus 2015) and respectively intercalate between nucleotide pairs +9 and +10 and −1 and −2 of the mRNA, exclusively in the intermediate states of translocation. Those two residues are thought to prevent a back-sliding of the mRNA during back-rotation of the 30S head, thus exerting a pawl function. In the post-translation state, however, the two intercalating nucleotides do not touch the mRNA. Residue C1397 has been described as being able to adopt multiple conformations in several crystal structures, in response to the presence of a tRNA at the A-site (Jenner et al. 2010) (Zhou et al. 2013). The comparison of our ambient and cryogenic temperature structures therefore illustrates the intrinsic flexible nature of C1397 even in the presence of tRNA at the A-site. It is beyond the scope of this work to pinpoint the exact cause of this small discrepancy between the datasets, although we consider some potential explanations. It seems counter-intuitive that the dataset collected at ambient temperature displays a more ordered mRNA channel, as Brownian motion of the molecules is dampened. However, the lack of structural radiation damage in SFX data may account for this finding. If radiation damage was an issue, however, differences between the two structures would be expected globally rather than only at this specific site. Even though temperature does not seem to explain the difference directly, there is a possibility that it does so indirectly, as the cryo-cooling process needed a higher concentration of cryo-protectant in the crystallization buffer. During cryogenic data collection experiment, the MPD concentration of mother liquor adjusted to 26% compared to 17% in the native buffer used in SFX experiment. Such an increase affects the hydration state of the crystal and, more importantly, results in a decrease of the dielectric constant of the solvent, thereby increasing the repulsive effect between like charges (Hanson et al. 2003). The density of negative charges in the mRNA channel, together with the more labile nature of the 3' end of the short mRNA fragment, might make this moiety more sensitive to this change in dielectric property of the solvent medium and account for the more-disordered state in the dataset collected at cryogenic temperature. Along similar lines, it is also possible that the electrokinetic injection method used to collect the ambient temperature dataset had an impact on the electrostatic state of the crystal.

Ambient-temperature studies build upon previous cryo-crystallography data

The low RMS deviation between the crystal structures collected in this work and its equivalent studied at cryogenic temperature suggests that previous structural data captures the 30S ribosomal subunit in a representative conformation. These data also illustrate the benefit of collecting data at ambient temperature if radiation damage can be outrun, since more structural details can be resolved in the mRNA channel of

177 the ribosome. The structure reported here builds on previous reports (Sierra et al. 2016) of serial
178 crystallography experiments involving microcrystals of fragile and large-molecular-weight targets using a
179 liquid-injector driven system. The time needed for data collection, four hours, makes such experiments
180 feasible within a few hours of precious beamtime, and can be further reduced with improvements in real-
181 time data processing and the use of high-repetition-rate sources such as European XFEL which has
182 recently commenced user operation.
183
184 A major promise of structural studies performed at ambient temperature is the ability to probe biological
185 macromolecules as they undergo reactions. Time-resolved SFX is an emerging approach that builds on the
186 successes of SFX in determining static structures and has been demonstrated for photo-sensitive targets
187 (Tenboer et al. 2014; Pande et al. 2016), with a time resolution as short as 100 fs. Methods to process data
188 from these experiments are rapidly improving (Spence 2017). Experimental approaches to mix enzymes
189 with their substrates on relevant enzymatic time scales in real-time prior to their delivery to the X-ray
190 beam are under development and would enabling the probing of structural intermediates of these enzymes
191 (Kupitz et al. 2017). The first demonstration of time-resolved structural enzymology at an XFEL has been
192 performed on a riboswitch and its substrate with a mixing time of 10 second (Stagno et al. 2017), paving
193 the way to performing similar experiments on ribonucleo-protein complexes such as the ribosome. Time-
194 resolved studies of the ribosome decoding complexes could potentially elucidate the process of decoding
195 to a level of clarity not previously attainable and answer key questions about the structural basis of
196 decoding dynamics.
197
198 **MATERIALS AND METHODS**
199
200 **Preparation and Crystallization of 30S Ribosomal Subunits for SFX crystallography at an XFEL**
201 30S ribosomal subunits from *T. thermophilus* HB8 (ATCC27634)(Yoshizaki et al. 1971) were prepared as
202 previously described (Wimberly et al. 2000; Demirci et al. 2010). Purified 30S ribosomal subunits were
203 crystallized at 4 ºC by the hanging drop method using a mother liquor solution containing 17% (v/v) 2-
204 methyl-2,4-pentanediol (MPD), 15 mM magnesium acetate, 200 mM potassium acetate, 75 mM
205 ammonium acetate and 100 mM 2-(*N*-morpholino) ethanesulfonic acid (MES)-KOH (pH 6.5). The mRNA
206 fragment (with codon sequences underlined), 5'<u>UUU</u>UUU3' and the anticodon stem loop ASL_{Phe}, (with
207 anticodon sequence underlined GGGGAUU<u>GAA</u>AAUCCCC, were purchased from Dharmacon (GE Life
208 Sciences). Microcrystals 2 × 2 × 4 μm^3 in size were harvested in the same mother liquor composition,
209 pooled (total volume of 500 µl loaded) and supplemented with 200µM of mRNA oligomer, ASL_{Phe} and 80
210 µM paromomycin for 48 hours before data collection. The crystal concentration was approximated to be

211 10^{10}-10^{11} particles per ml based on light microscopy and nanoparticle tracking analysis (NanoSight LM10-
212 HS with corresponding Nanoparticle Tracking Analysis (NTA) software suite (Malvern Instruments,
213 Malvern, UK).
214
215 **coMESH construction**
216 The concentric microfluidic electrokinetic sample holder (coMESH), which is the liquid injector used to
217 deliver the microcrystals to the X-ray beam, is comprised of two capillaries: one large and one small. The
218 central, smaller capillary carrying the microcystals of the 30S decoding complex was a continuous fused
219 silica capillary of 100 μm inner diameter, 160 μm outer diameter, and 1.5 m length (Polymicro, Phoenix,
220 AZ, USA). This capillary directly connected the sample reservoir with the X-ray interaction region,
221 passing through a vacuum feedthrough and then through a microfluidic *Interconnect Cross* (C360-204,
222 LabSmith, Livermore, CA USA; C360-203 *Interconnect Tee* may also be used with no need to plug the
223 fourth channel) (Fig. 1A). The uninterrupted, straight capillary was free of in-line filters, unions or any
224 other connections, thus minimizing the risk of sample clogs and leaks, which most often occur at flow
225 channel transitions. A similar uninterrupted approach was used for the larger capillary. The fitting at the
226 top of the *cross* in Figure 1A was an adapter fitting (T116-A360 as well as T116-100, LabSmith,
227 Livermore, CA, USA) which compressed a 1/16" (1.6 mm) OD, 0.007" (178 μm) ID polymer (FEP)
228 tubing sleeve (F-238, Upchurch, Oak Harbor, WA, USA) onto the sample capillary. This connection
229 method was necessary to properly seal the capillary to the *cross*. The sheath line at the bottom of the figure
230 was a short 5 cm fused silica capillary with an outer diameter of 360 µm and an inner diameter of 180,
231 200, or 250 μm depending on the desired flow rate of the sheath liquid at a given driving pressure. This
232 outer capillary was connected to the *cross*, and the sheath liquid was supplied from the third port of the
233 cross (the left port in the figure) through a compatible microfluidic tubing; we typically used silica
234 capillaries with 360 μm outer diameters and 200 μm inner diameters for optimum flow rate. For simplicity,
235 the injector has been designed to operate at relatively low backing pressures (up to a few atmospheres). For
236 this experiment, the sheath liquid line was connected to a syringe filled with the appropriate sister liquor
237 which contains the cryoprotection solution, driven by a syringe pump (PHD Ultra, 703006, Harvard
238 Apparatus, Holliston, MA, USA) We electrically charged the sheath liquid between 0-5,000 V potential
239 using an in-line conductive charging union (M-572, Upchurch, Oak Harbor, WA, USA) connected to a
240 SRS PS350 (Stanford Research Systems, Sunnyvale, CA, USA) high voltage source.
241 The capillary assembly was loaded into a vacuum chamber with 1×1 μm^2 focused XFEL beam
242 and the standard load-lock system of the CXI instrument. A grounded, conical counter electrode with a 1
243 cm opening was placed approximately 5 mm below the capillary tip; the capillaries and opening of the

244 cone were coaxial. The angle of the cone and its distance from the tip were set to enable a diffraction cone
245 with a 45° 2q scattering angle. All capillaries were fed through vacuum flanges with 1/16" (1.6 mm)
246 Swagelok bulkhead fittings using appropriately sized polymer sleeves. The sheath reservoir was a 1 ml
247 Gastight Hamilton syringe with a PTFE Luer tip (1001 TLL SYR, Hamilton, USA). The ribosome
248 microcrystalline sample was supplied from a 500 μl Hamilton Gastight syringe.
249

250 **Selecting a sister liquor for the ribosome microcrystalline slurry**

251 The coMESH incorporates a "sister liquor" as part of its sample delivery design which is used to protect
252 the microcrystals and their mother liquor from the dehydrative effects of the sample chamber vacuum (10^{-}
253 ^{5} Torr). This fluid travels in the larger capillary and, after reaching the cross, peripherally to the sample
254 line until the terminus of the capillary within the sample chamber. The choice of fluid may reflect the
255 composition of the crystals' mother liquor but need not strictly match it. For delivery of ribosome
256 microcrystals using co-terminal capillaries (Sierra et al. 2016), the compatibility between the sister liquor
257 and the ribosome crystals was not considered since fluid interaction occurred immediately prior to
258 reaching the X-ray interaction region, allowing minimal time, if any, for the fluids to mix. Current and
259 prior experimental experience suggest that a 26% MPD-containing sister liquor seems to be an ideal choice
260 for co-terminal sample delivery. The buffer has proven to be quite reliable, surviving injection into
261 vacuum with minimal issues especially with respect to buildup of dehydrated precipitates, which can occur
262 with salts or polyethylene glycols and is problematic for sample delivery due to its adherence to (and thus,
263 blockage of) the capillary tip. Other factors influencing the choice of fluid include availability of the fluid
264 and its viscosity. The lower viscosity allows the sister liquor to be pumped easily by a standard syringe
265 pump through the more resistive *cross* manifold or concentric annular flow before the exit region of the
266 capillary.
267

268 **Operation of the coMESH**

269 Before connecting the central sample line, the sister liquor was loaded, flowed and electrically focused.
270 Once a slightly stable jet was achieved, the central sample line carrying ribosome slurry was connected.
271 Notably, the sister liquor never fully stabilized because of the entrained air from the disconnected sample
272 line continuously introducing bubbles. The central sample line had much less fluidic resistance compared
273 to the outer line; connecting it first with a vacuum sensitive sample will cause immediate jet clogging and
274 blockages, for this reason the outer line should always be on while operating in vacuum environment. In
275 general, the sister liquor was set to flow at or near the flow rate of the mother liquor. If diffraction hits

were not observed, the sister liquor flow was reduced and/or the mother liquor flow was increased slowly (to ensure stable jetting) until diffraction patterns reappeared.

Ribosome microcrystalline sample injection with coMESH

For the study of 30S-mRNA-ASL-paromomycin complex crystals, the inner sample line contained unfiltered crystals in their native mother liquor containing 17% (v/v) 2-methyl-2,4-pentanediol (MPD). The size distribution of the 30S crystals was uniform owing to their controlled slower growth at 4°C (Demirci et al. 2013b). Occasional larger-sized 30S crystals were discarded by repeated gentle differential settling without centrifugation. The outer sister liquor was the same buffer, with no crystals, as the mother liquor in that the original substituent concentrations remained constant while having increased the MPD to 26% (v/v) to aid in-vacuum injection.

Data collection and analysis for SFX studies at LCLS

The serial femtosecond X-ray crystallography (SFX) experiment was performed at Coherent X-ray Imaging instrument (CXI) of the Linac Coherent Light Source (LCLS; SLAC National Accelerator Laboratory, Menlo Park, CA, USA) under beamtime ID: cxil1416. The LCLS X-ray beam with a pulse duration of approximately 50 fs was focused using X-ray optics in a Kirkpatrick-Baez geometry to a beam size of $1.3 \times 1.3\ \mu m^2$ full width at half maximum (FWHM) at a pulse energy of 2.9 mJ, a photon energy of 9.5 keV (1.29 Å) and a repetition rate of 120 Hz.

A total of 1,731,280 images were collected with the Cornell-SLAC Pixel Array Detector (CSPAD) (Pietrini and Nettelblad 2017) from crystals of the 30S-mRNA-ASL-paromomycin complex. The total beamtime used for this dataset was 240 minutes (out of an available 360 minutes). Crystal hits were defined as frames containing more than 30 Bragg peaks with a minimum signal-to-noise ratio greater than 4.5 on each detector image, for a total of 165,954 hits. The detector distance was set to 223 mm, with an achievable resolution of 3.08 Å at the edge of the detector (2.6 Å in the corner).

After the detection of crystal hits and following the conversion of individual diffraction patterns to the HDF5 format by *CHEETAH* (Barty et al. 2014), the *CrystFEL* software suite (White et al. 2016) was used for crystallographic analysis. The information of peak positions was used for the indexing of individual, randomly oriented crystal diffraction patterns using FFT-based indexing approaches. The detector geometry was refined using an automated algorithm to match found and predicted peaks to subpixel accuracy (Yefanov et al. 2015). The integration step was performed using a built-in Monte-Carlo algorithm to estimate accurate structure factors from thousands of individually measured Bragg peaks (Kirian et al.

310 2010). After the application of per-pattern resolution cutoff, frames which did not match to an initial
311 merged dataset with a Pearson correlation coefficient of less than 0.4, were excluded from the final dataset.
312 Diffraction intensities from a total of 19,374 indexed diffraction patterns (11.8 % indexing rate) were
313 merged into a final dataset (Overall CC* = 0.93; 3.45 Å cutoff) for further analysis ($P4_12_12$, unit cell: a = b
314 = 402.3 Å, c = 176.4 Å; α = β = γ = 90°). The final resolution cutoff was estimated to be 3.45 Å using a
315 combination of *CC1/2* (Karplus and Diederichs 2012) and other refinement parameters. The final dataset
316 had an overall R_{split} = 63.3% and CC^* = 0.36 in the highest resolution shell.
317
318 **Ambient temperature 30S Ribosomal Subunit SFX Structure refinement**
319 We determined the ambient temperature structure of the 30S-mRNA-ASL-paromomycin complex using
320 the automated molecular replacement program *PHASER* (McCoy et al. 2007) with the previously
321 published cryo-cooled 30S ribosomal subunit-mRNA-ASL-paromomycin complex synchrotron structure
322 as a search model (PDB entries 4DR4 and 1IBL)(Ogle et al. 2001; Demirci et al. 2013a). The resulting
323 structure was refined with rRNA modifications, which are mostly located near the decoding center. This
324 choice of starting search model minimized experimental variations between the two structures such as
325 sample preparation, crystal growth, data processing, and model registry. Coordinates of the 4DR4 with
326 additional RNA and protein modifications were used for the initial rigid body refinement with the *PHENIX*
327 software package (Adams et al. 2010). During the initial refinement of ambient temperature XFEL
328 structure, the entire mRNA and ASL components were omitted and the new models were built into
329 unbiased difference density. After simulated-annealing refinement, individual coordinates, three group B
330 factors per residue, and TLS parameters were refined. Potential positions of magnesium or potassium ions
331 were compared with those in the high-resolution (2.5 Å) 30S subunit structure (PDB accession code
332 2VQE), in program *COOT* (Emsley and Cowtan 2004), and positions with strong difference density were
333 retained. All magnesium atoms were replaced with magnesium hexahydrate. Water molecules located
334 outside of significant electron density were manually removed. The Ramachandran statistics for this
335 dataset (most favored / additionally allowed / generously allowed / disallowed) are 87.3 / 11.7 / 0.7 / 0.2 %
336 respectively. The structure refinement statistics are summarized in Table 1. Structure alignments were
337 performed using the alignment algorithm of *PyMOL* (www.schrodinger.com/pymol) with the default 2σ
338 rejection criterion and five iterative alignment cycles. All X-ray crystal structure figures were produced
339 with *PyMOL*.
340
341 **DATA DEPOSITION**
342 The coordinates have been deposited in the Protein Data Bank with the accession code 6CAO.
343

ACKNOWLEDGEMENTS

The authors thank Michelle Young for her support and critical reading of the manuscript. Portions of this research were carried out at the Linac Coherent Light Source (LCLS) at the SLAC National Accelerator Laboratory. Use of the LCLS is supported by the U.S. Department of Energy (DOE), Office of Science, Office of Basic Energy Sciences (OBES) under Contract No. DE-AC02-76SF00515. The LCLS is acknowledged for beam time access under experiment no. cxil1416. EHD, RGS and HD acknowledge the support of OBES through the AMOS program within the CSGB and the DOE through the SLAC Laboratory Directed Research and Development Program. EHD acknowledges financial support from the Stanford University Dean of Research. HD acknowledges support from NSF Science and Technology Centers grant NSF-1231306 (Biology with X-ray Lasers, BioXFEL). FP, NC and FPA are supported by National Institutes of Health (NIH) grant R35GM122543. Parts of the sample injector used at LCLS for this research was funded by the National Institutes of Health, P41GM103393, formerly P41RR001209. CG acknowledges SLAC and the DOE for financial support through the Panofsky fellowship. CDL acknowledges Stiftelsen JC Kempes Minnes Stipendiefond for financial support. We thank A. Fry's continuous support for LCLS intern students who contributed to the portions of the experiments carried at LCLS. H.D. acknowledges valuable discussions with A. Takeuchi, K. Dursuncan and E. Satunaz. We thank G. Stewart of SLAC for excellent technical assistance with creating graphics for Figure 1A.

Author contributions: HD and EHD designed the project. HD, EHD, YR, HC, FA prepared the samples for SFX studies. RGS, HD, AM, PM, BH, TO, CDL and EHD build the coMESH injectors. FP and CG executed the SFX data reduction. NC and FPA provided realtime XFEL data analysis. HD refined the structure. The experiments were executed by HD, EHD, RGS, FP, NC, FPA, MH, ML, MS, FA, HIC, LZ, YR. Data were analyzed by HD, EHD, FP, SW, CG and RGS. The manuscript was prepared by HD, EHD, FP, CG, SW and RGS with input from all the coauthors.

REFERENCES

Achenbach J, Nierhaus KH. 2015. The mechanics of ribosomal translocation. *Biochimie* **114**: 80-89.

Adams PD, Afonine PV, Bunkoczi G, Chen VB, Davis IW, Echols N, Headd JJ, Hung LW, Kapral GJ, Grosse-Kunstleve RW et al. 2010. PHENIX: a comprehensive Python-based system for macromolecular structure solution. *Acta Crystallogr D Biol Crystallogr* **66**: 213-221.

Allred BE, Gebala M, Herschlag D. 2017. Determination of Ion Atmosphere Effects on the Nucleic Acid Electrostatic Potential and Ligand Association Using AH(+).C Wobble Formation in Double-Stranded DNA. *J Am Chem Soc* **139**: 7540-7548.

Anthony PC, Sim AY, Chu VB, Doniach S, Block SM, Herschlag D. 2012. Electrostatics of nucleic acid folding under conformational constraint. *J Am Chem Soc* **134**: 4607-4614.

383 Ban N, Nissen P, Hansen J, Moore PB, Steitz TA. 2000. The complete atomic structure of the
384 large ribosomal subunit at 2.4 A resolution. *Science* **289**: 905-920.
385 Barty A, Kirian RA, Maia FR, Hantke M, Yoon CH, White TA, Chapman H. 2014. Cheetah:
386 software for high-throughput reduction and analysis of serial femtosecond X-ray
387 diffraction data. *J Appl Crystallogr* **47**: 1118-1131.
388 Ben-Shem A, Garreau de Loubresse N, Melnikov S, Jenner L, Yusupova G, Yusupov M. 2011.
389 The structure of the eukaryotic ribosome at 3.0 A resolution. *Science* **334**: 1524-1529.
390 Demirci H, Murphy Ft, Belardinelli R, Kelley AC, Ramakrishnan V, Gregory ST, Dahlberg AE,
391 Jogl G. 2010. Modification of 16S ribosomal RNA by the KsgA methyltransferase
392 restructures the 30S subunit to optimize ribosome function. *RNA* **16**: 2319-2324.
393 Demirci H, Murphy Ft, Murphy E, Gregory ST, Dahlberg AE, Jogl G. 2013a. A structural basis for
394 streptomycin-induced misreading of the genetic code. *Nat Commun* **4**: 1355.
395 Demirci H, Sierra RG, Laksmono H, Shoeman RL, Botha S, Barends TR, Nass K, Schlichting I,
396 Doak RB, Gati C et al. 2013b. Serial femtosecond X-ray diffraction of 30S ribosomal
397 subunit microcrystals in liquid suspension at ambient temperature using an X-ray free-
398 electron laser. *Acta Crystallogr Sect F Struct Biol Cryst Commun* **69**: 1066-1069.
399 Emsley P, Cowtan K. 2004. Coot: model-building tools for molecular graphics. *Acta Crystallogr D*
400 *Biol Crystallogr* **60**: 2126-2132.
401 Evers U, Franceschi F, Boddeker N, Yonath A. 1994. Crystallography of halophilic ribosome: the
402 isolation of an internal ribonucleoprotein complex. *Biophys Chem* **50**: 3-16.
403 Fischer N, Neumann P, Konevega AL, Bock LV, Ficner R, Rodnina MV, Stark H. 2015. Structure
404 of the E. coli ribosome-EF-Tu complex at <3 A resolution by Cs-corrected cryo-EM.
405 *Nature* **520**: 567-570.
406 Haas DJ, Rossmann MG. 1970. Crystallographic studies on lactate dehydrogenase at-75
407 degrees C. *Acta Crystallogr B* **26**: 998-1004.
408 Hagerman PJ. 1988. Flexibility of DNA. *Annu Rev Biophys Biophys Chem* **17**: 265-286.
409 -. 1990. Sequence-directed curvature of DNA. *Annu Rev Biochem* **59**: 755-781.
410 Hanson BL, Harp JM, Bunick GJ. 2003. The well-tempered protein crystal: annealing
411 macromolecular crystals. *Methods Enzymol* **368**: 217-235.
412 Jenner LB, Demeshkina N, Yusupova G, Yusupov M. 2010. Structural aspects of messenger
413 RNA reading frame maintenance by the ribosome. *Nat Struct Mol Biol* **17**: 555-560.
414 Karplus PA, Diederichs K. 2012. Linking crystallographic model and data quality. *Science* **336**:
415 1030-1033.
416 Kirian RA, Wang X, Weierstall U, Schmidt KE, Spence JC, Hunter M, Fromme P, White T,
417 Chapman HN, Holton J. 2010. Femtosecond protein nanocrystallography-data analysis
418 methods. *Opt Express* **18**: 5713-5723.
419 Korostelev A, Trakhanov S, Laurberg M, Noller HF. 2006. Crystal structure of a 70S ribosome-
420 tRNA complex reveals functional interactions and rearrangements. *Cell* **126**: 1065-1077.
421 Kupitz C, Olmos JL, Jr., Holl M, Tremblay L, Pande K, Pandey S, Oberthur D, Hunter M, Liang
422 M, Aquila A et al. 2017. Structural enzymology using X-ray free electron lasers. *Struct*
423 *Dyn* **4**: 044003.
424 Lebrun A, Shakked Z, Lavery R. 1997. Local DNA stretching mimics the distortion caused by the
425 TATA box-binding protein. *Proc Natl Acad Sci U S A* **94**: 2993-2998.
426 Liang M, Williams GJ, Messerschmidt M, Seibert MM, Montanez PA, Hayes M, Milathianaki D,
427 Aquila A, Hunter MS, Koglin JE et al. 2015. The Coherent X-ray Imaging instrument at
428 the Linac Coherent Light Source. *J Synchrotron Radiat* **22**: 514-519.
429 Lipfert J, Doniach S, Das R, Herschlag D. 2014. Understanding nucleic acid-ion interactions.
430 *Annu Rev Biochem* **83**: 813-841.
431 Loveland AB, Demo G, Grigorieff N, Korostelev AA. 2017. Ensemble cryo-EM elucidates the
432 mechanism of translation fidelity. *Nature* **546**: 113-117.

433 McCoy AJ, Grosse-Kunstleve RW, Adams PD, Winn MD, Storoni LC, Read RJ. 2007. Phaser
434 crystallographic software. *J Appl Crystallogr* **40**: 658-674.
435 Mitra K, Schaffitzel C, Shaikh T, Tama F, Jenni S, Brooks CL, 3rd, Ban N, Frank J. 2005.
436 Structure of the E. coli protein-conducting channel bound to a translating ribosome.
437 *Nature* **438**: 318-324.
438 Moazed D, Noller HF. 1989. Intermediate states in the movement of transfer RNA in the
439 ribosome. *Nature* **342**: 142-148.
440 Natchiar SK, Myasnikov AG, Kratzat H, Hazemann I, Klaholz BP. 2017. Visualization of chemical
441 modifications in the human 80S ribosome structure. *Nature* **551**: 472-477.
442 Noller HF. 2013. By ribosome possessed. *J Biol Chem* **288**: 24872-24885.
443 Ogle JM, Brodersen DE, Clemons WM, Jr., Tarry MJ, Carter AP, Ramakrishnan V. 2001.
444 Recognition of cognate transfer RNA by the 30S ribosomal subunit. *Science* **292**: 897-
445 902.
446 Ogle JM, Carter AP, Ramakrishnan V. 2003. Insights into the decoding mechanism from recent
447 ribosome structures. *Trends Biochem Sci* **28**: 259-266.
448 Pande K, Hutchison CD, Groenhof G, Aquila A, Robinson JS, Tenboer J, Basu S, Boutet S,
449 DePonte DP, Liang M et al. 2016. Femtosecond structural dynamics drives the trans/cis
450 isomerization in photoactive yellow protein. *Science* **352**: 725-729.
451 Peters JP, 3rd, Maher LJ. 2010. DNA curvature and flexibility in vitro and in vivo. *Q Rev Biophys*
452 **43**: 23-63.
453 Petrov A, Kornberg G, O'Leary S, Tsai A, Uemura S, Puglisi JD. 2011. Dynamics of the
454 translational machinery. *Curr Opin Struct Biol* **21**: 137-145.
455 Pietrini A, Nettelblad C. 2017. Artifact reduction in the CSPAD detectors used for LCLS
456 experiments. *J Synchrotron Radiat* **24**: 1092-1097.
457 Schluenzen F, Tocilj A, Zarivach R, Harms J, Gluehmann M, Janell D, Bashan A, Bartels H,
458 Agmon I, Franceschi F et al. 2000. Structure of functionally activated small ribosomal
459 subunit at 3.3 angstroms resolution. *Cell* **102**: 615-623.
460 Schuwirth BS, Borovinskaya MA, Hau CW, Zhang W, Vila-Sanjurjo A, Holton JM, Cate JH. 2005.
461 Structures of the bacterial ribosome at 3.5 A resolution. *Science* **310**: 827-834.
462 Selmer M, Dunham CM, Murphy FVt, Weixlbaumer A, Petry S, Kelley AC, Weir JR,
463 Ramakrishnan V. 2006. Structure of the 70S ribosome complexed with mRNA and tRNA.
464 *Science* **313**: 1935-1942.
465 Sierra RG, Gati C, Laksmono H, Dao EH, Gul S, Fuller F, Kern J, Chatterjee R, Ibrahim M,
466 Brewster AS et al. 2016. Concentric-flow electrokinetic injector enables serial
467 crystallography of ribosome and photosystem II. *Nat Methods* **13**: 59-62.
468 Spence JCH. 2017. XFELs for structure and dynamics in biology. *IUCrJ* **4**: 322-339.
469 Stagno JR, Liu Y, Bhandari YR, Conrad CE, Panja S, Swain M, Fan L, Nelson G, Li C, Wendel
470 DR et al. 2017. Structures of riboswitch RNA reaction states by mix-and-inject XFEL
471 serial crystallography. *Nature* **541**: 242-246.
472 Tan ZJ, Chen SJ. 2011. Salt contribution to RNA tertiary structure folding stability. *Biophys J*
473 **101**: 176-187.
474 Tenboer J, Basu S, Zatsepin N, Pande K, Milathianaki D, Frank M, Hunter M, Boutet S, Williams
475 GJ, Koglin JE et al. 2014. Time-resolved serial crystallography captures high-resolution
476 intermediates of photoactive yellow protein. *Science* **346**: 1242-1246.
477 Warkentin M, Hopkins JB, Haber JB, Blaha G, Thorne RE. 2014. Temperature-dependent
478 radiation sensitivity and order of 70S ribosome crystals. *Acta Crystallogr D Biol*
479 *Crystallogr* **70**: 2890-2896.
480 White TA, Mariani V, Brehm W, Yefanov O, Barty A, Beyerlein KR, Chervinskii F, Galli L, Gati C,
481 Nakane T et al. 2016. Recent developments in CrystFEL. *J Appl Crystallogr* **49**: 680-689.

482 Wimberly BT, Brodersen DE, Clemons WM, Jr., Morgan-Warren RJ, Carter AP, Vonrhein C,
483 Hartsch T, Ramakrishnan V. 2000. Structure of the 30S ribosomal subunit. *Nature* **407**:
484 327-339.
485 Yefanov O, Mariani V, Gati C, White TA, Chapman HN, Barty A. 2015. Accurate determination of
486 segmented X-ray detector geometry. *Opt Express* **23**: 28459-28470.
487 Yoshizaki F, Oshima T, Imahori K. 1971. Studies on phosphoglucomutase from an extreme
488 thermophile, Flavobacterium thermophilum HB8. I. Thermostability and other enzymatic
489 properties. *J Biochem* **69**: 1083-1089.
490 Yoshizawa S, Fourmy D, Puglisi JD. 1999. Recognition of the codon-anticodon helix by
491 ribosomal RNA. *Science* **285**: 1722-1725.
492 Yusupov MM, Yusupova GZ, Baucom A, Lieberman K, Earnest TN, Cate JH, Noller HF. 2001.
493 Crystal structure of the ribosome at 5.5 A resolution. *Science* **292**: 883-896.
494 Yusupova G, Jenner L, Rees B, Moras D, Yusupov M. 2006. Structural basis for messenger
495 RNA movement on the ribosome. *Nature* **444**: 391-394.
496 Zhou J, Lancaster L, Donohue JP, Noller HF. 2013. Crystal structures of EF-G-ribosome
497 complexes trapped in intermediate states of translocation. *Science* **340**: 1236086.
498

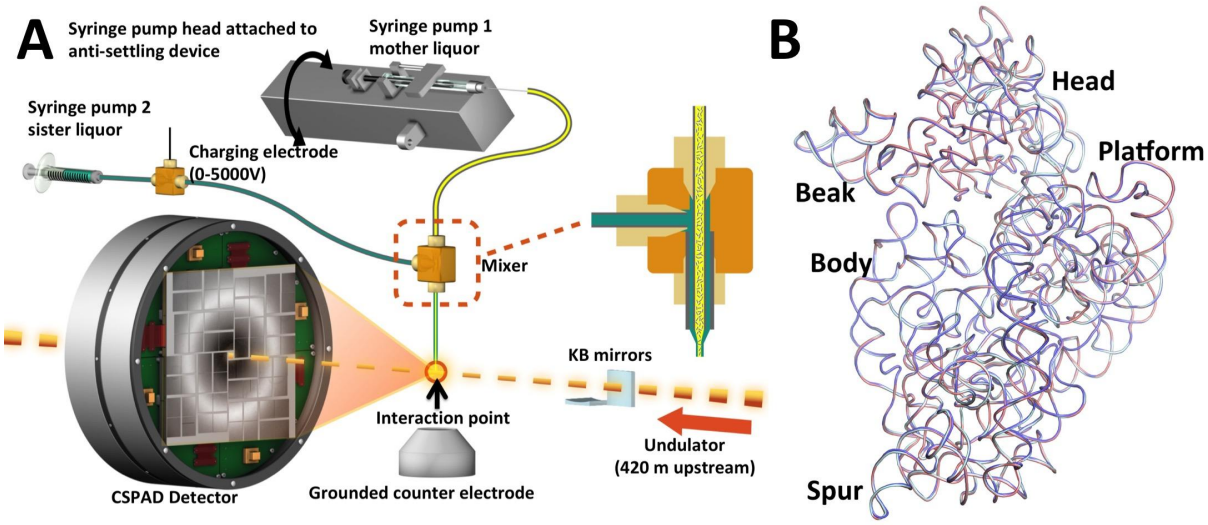

FIGURE 1. Serial Femtosecond X-ray (SFX) crystallography studies of 30S ribosomal subunit decoding complexes (A) Diagram of the concentric-flow MESH injector setup at the CXI instrument of the LCLS. The liquid jet, comprising microcrystals and their mother liquor (colored in yellow), flows in the continuous inner capillary (100 μm × 160 μm × 1.5 m; colored in gray). The sister liquor (colored in green) is charged by a high voltage power supply (0-5,000 V) for electro-focusing of the liquid jet. A mixer (indicated within the dashed orange rectangle) joins the two capillaries (colored in gray) concentrically. The sample reservoir containing ribosome microcrystals is mounted on an anti-settling device, which rotates, at an angle, about the capillary axis to keep the microcrystals suspended homogenously in the slurry. The liquid jet and the LCLS pulses interact at the point indicated by the orange circle. (B) Comparison of *T. thermophilus* 30S-ASL-mRNA-paromomycin complex structures. Superposition of 16S rRNA backbones from cryo-cooled structures colored in cyan and slate PDB IDs: 4DR4 and1IBL respectively with ambient temperature structure colored in salmon. The positions of the major 30S domains are indicated. All X-ray crystal structure figures are produced with PyMOL (http://www.schrodinger.com/pymol).

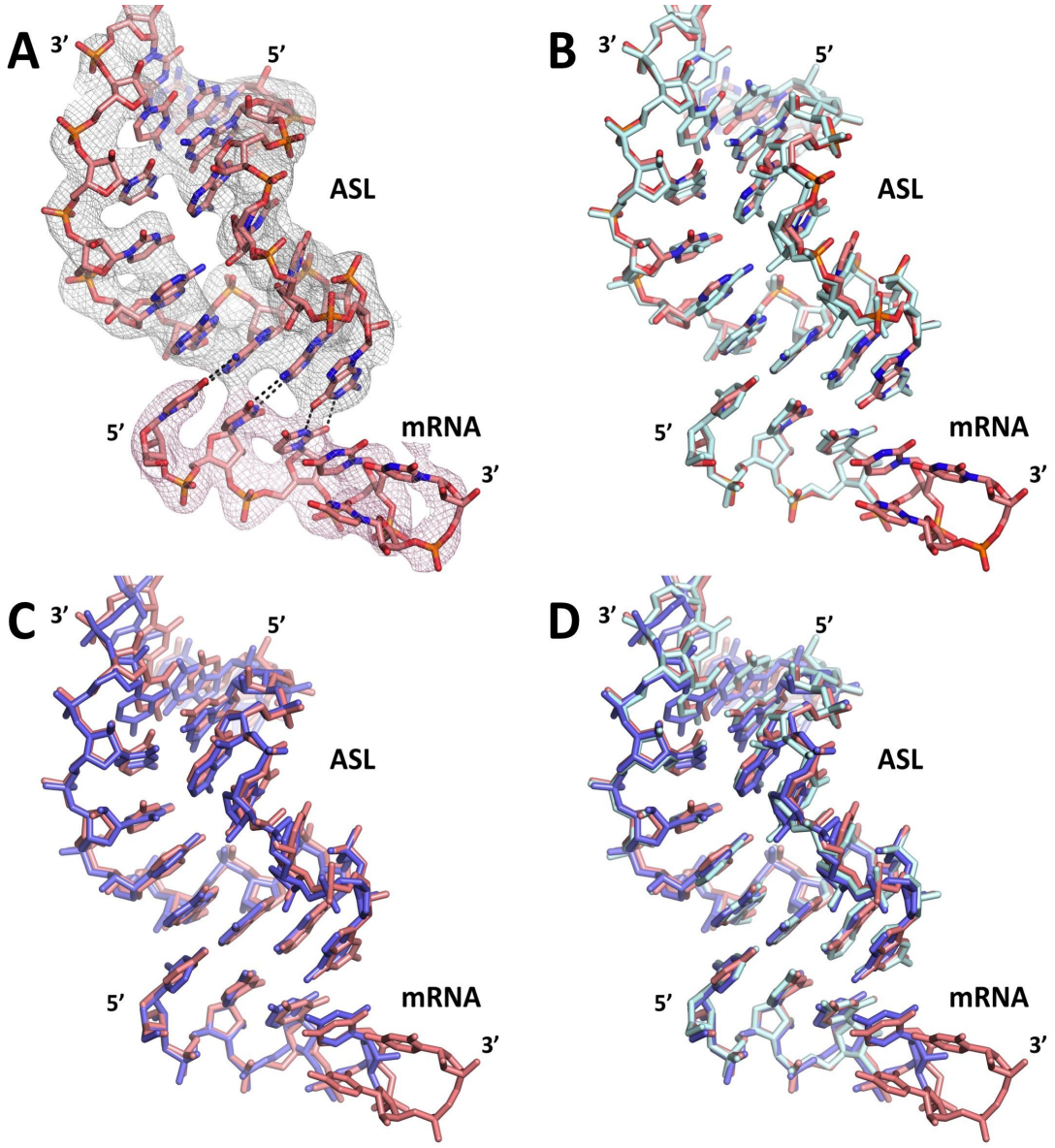

FIGURE 2. Structural comparison of ambient and cryogenic temperature decoding complexes. (A) Final unbiased Fo-Fc simple omit ambient temperature electron-density map of mRNA and ASL contoured at the 3 σ level, colored in gray and shown at 3 Å. (B) Superposition of the ambient (salmon) and cryo (cyan) temperature structures from our group showing the agreement between them. (C) Superposition of our ambient temperature structure (salmon) and the identical cryo temperature structure obtained by another laboratory (slate) (PDB ID 1IBL) showing the agreement between them. (D) Superposition of our ambient temperature structure (salmon) with the two cryo structures (cyan and slate).

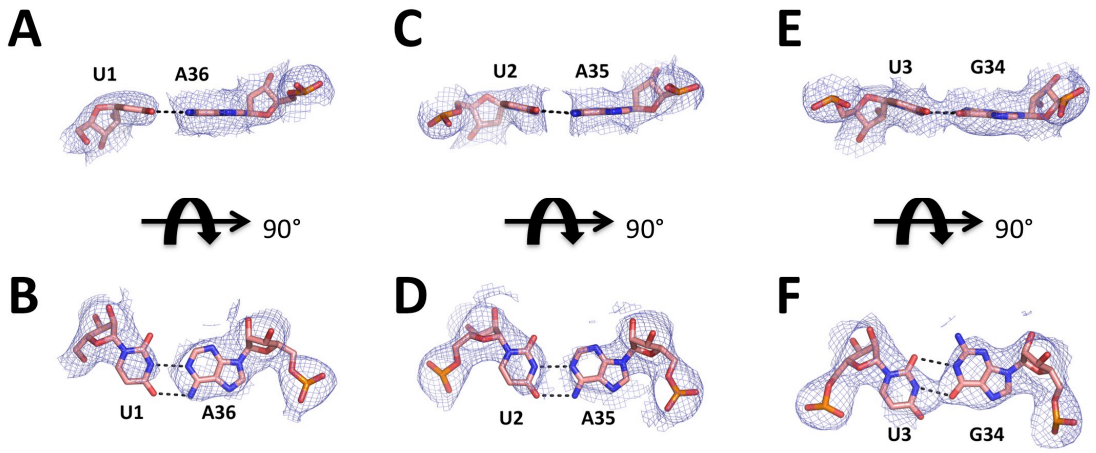

FIGURE 3. X-ray crystallography structures of the decoding mRNA-ASL minihelix. (A) Simple F_o-F_c omit maps of the decoding complex individual base pair mRNA(U1)-ASL(A36) contoured at the 3 σ level, colored in gray and shown at 3 Å. (B) same as A rotated around x-axis by 90 degrees. (C) Simple F_o-F_c omit maps of the decoding complex individual base pair mRNA(U2)-ASL(A35) contoured at the 3 σ level, colored in gray and shown at 3 Å. (D) same as C rotated around x-axis by 90 degrees. (E) Simple F_o-F_c omit maps of the decoding complex individual base pair mRNA(U3)-ASL(G34) contoured at the 3 σ level, colored in gray and shown at 3 Å. (E) same as C rotated around x-axis by 90 degrees.

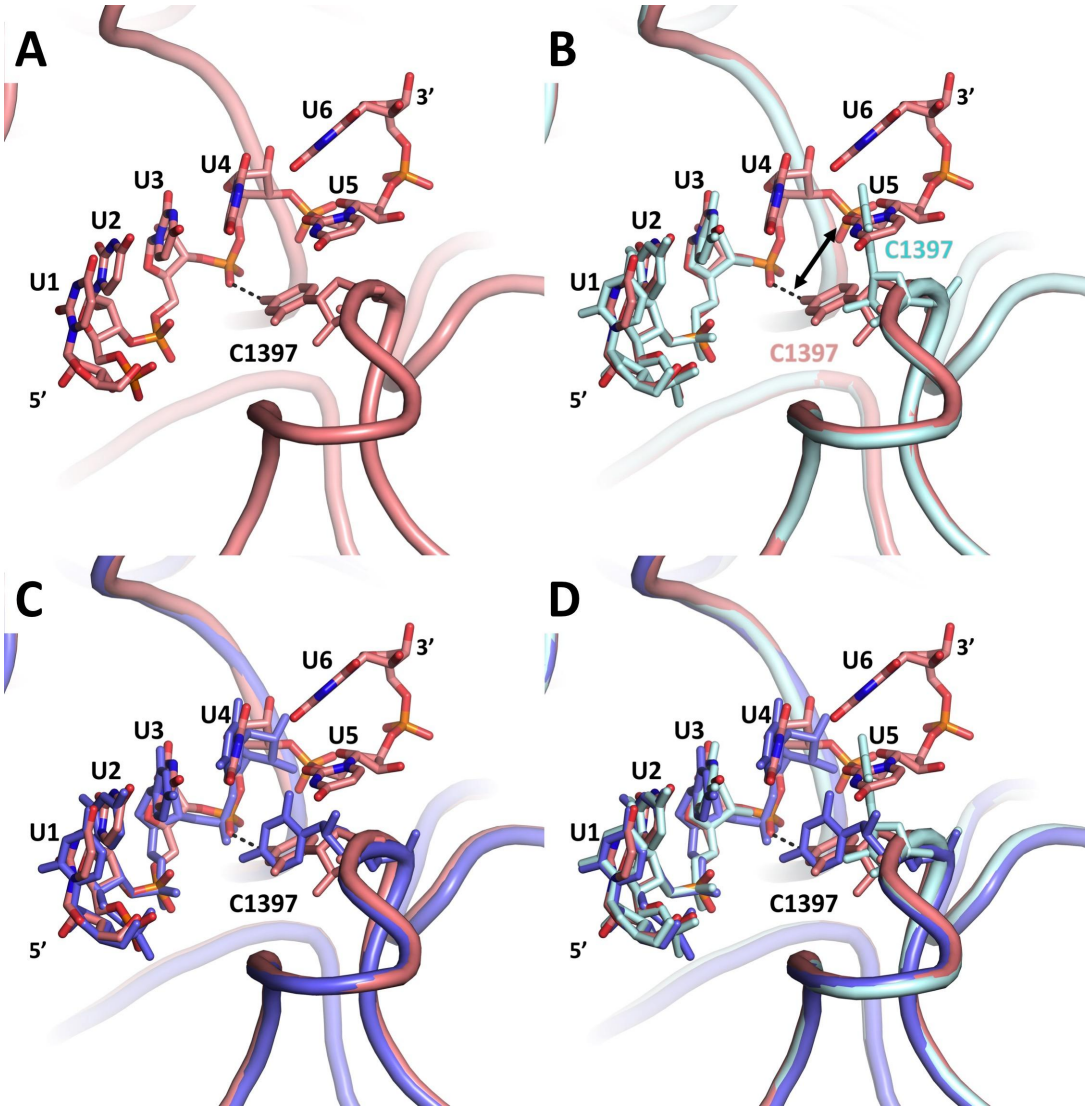

FIGURE 4. Temperature dependence of C1397 conformational dynamics. (A) Ambient temperature mRNA model at the decoding region. C1397 engages in H-bonding with U4 which demarcates the boundary between the A-site mRNA codon and codon -1. (B) Superposition of the ambient temperature 30S-decoding complex with cryogenic structure shows the disorder in the cryogenic mRNA structure also the alternate conformation of the C1397. (C) Superposition of our ambient temperature structure (salmon) and the identical cryo temperature structure obtained by another laboratory (slate) (PDB ID 1IBL) showing the disorder in the cryogenic structure. (D) Superposition of our ambient temperature structure (salmon) with the two cryo structures (cyan and slate).

Table 1. Data collection and refinement statistics

	30S SFX decoding complex
Data collection	PDB ID (6CAO)
Beamline	LCLS (CXI)
Space group	$P4_12_12$
Cell dimensions	
a, *b*, *c* (Å)	402.3, 402.3, 176.4
α, β, γ (°)	90, 90, 90
Resolution (Å)	30.0-3.45 (3.51-3.45)*
R_{split}	63.3 (229.2)
I / σ(I)	5.89 (0.89)
Completeness (%)	100 (100)
Multiplicity	384.7 (250.6)
CC (1/2)	0.93 (0.36)
Refinement	
Resolution (Å)	30.0-3.45 (3.63-3.45)
No. reflections	188443 (26462)
R_{work} / R_{free}	0.21/0.27 (0.30/0.35)
No. atoms	
Protein	19109
RNA	32504
Ligand/ion	1242
B-factors (Å^2)	
Protein	92.9
RNA	84.2
Ligand/ion	104.6
Coordinate error	0.63
R.m.s. deviations	
Bond lengths (Å)	0.006
Bond angles (°)	0.995
Ramachandran plot	
Favored (%)	87.3
Allowed (%)	11.7
Generously allowed (%)	0.7
Disallowed (%)	0.2

* Values in parentheses are for highest-resolution shell.